ADVANCED MATERIALS
www.advmat.de

# 3D Soft Architectures for Stretchable Thermoelectric Wearables with Electrical Self-Healing and Damage Tolerance

*Youngshang Han, Halil Tetik, and Mohammad H. Malakooti**

**Flexible thermoelectric devices (TEDs) exhibit adaptability to curved surfaces, holding significant potential for small-scale power generation and thermal management. However, they often compromise stretchability, energy conversion, or robustness, thus limiting their applications. Here, the implementation of 3D soft architectures, multifunctional composites, self-healing liquid metal conductors, and rigid semiconductors is introduced to overcome these challenges. These TEDs are extremely stretchable, functioning at strain levels as high as 230%. Their unique design, verified through multiphysics simulations, results in a considerably high power density of 115.4 µW cm$^{-2}$ at a low-temperature gradient of 10 °C. This is achieved through 3D printing multifunctional elastomers and examining the effects of three distinct thermal insulation infill ratios (0%, 12%, and 100%) on thermoelectric energy conversion and structural integrity. The engineered structure is lighter and effectively maintains the temperature gradient across the thermoelectric semiconductors, thereby resulting in higher output voltage and improved heating and cooling performance. Furthermore, these thermoelectric generators show remarkable damage tolerance, remaining fully functional even after multiple punctures and 2000 stretching cycles at 50% strain. When integrated with a 3D-printed heatsink, they can power wearable sensors, charge batteries, and illuminate LEDs by scavenging body heat at room temperature, demonstrating their application as self-sustainable electronics.**

## 1. Introduction

Thermoelectric devices (TEDs) reversibly convert heat and electricity based on the Seebeck and Peltier effects. Macro-TEDs, ranging from 1 to 30 cm$^2$ in size, are low-maintenance transducers that offer power generation and thermal management in noise-free, vibration-free, and prolonged operations.[1,2] For emerging applications like self-powered wearable electronics,[3] thermo-haptics,[4] and personalized thermoregulation,[5] the TEDs must be highly flexible or stretchable to provide effective heat transfer and energy conversion by maintaining conformal contact with curved surfaces. However, achieving the desired stretchability in thermoelectrics without compromising their performance remains a technological challenge.

Embedding inorganic rigid thermoelectric (TE) materials in silicone elastomers is an effective approach to fabricate flexible TEDs.[6,7] The TE pellets are arranged in a $\pi$-shaped configuration consisting of n-type and p-type thermoelectric legs, allowing for effective thermoelectric energy conversion, while the surrounding elastomer provides mechanical flexibility.[8,9] Due to the high Seebeck coefficient of inorganic TE materials and the separation of the hot and cold sides, this approach shows greater energy conversion compared to organic semiconductors and thin-film device configurations. More recently, stretchable TEDs have emerged through innovative solutions like 3D helical structure.[10] and gallium-based liquid metal (LM) interconnects.[11] In such devices, either the wavy structure of thin films or the fluidity of LM conductors enables elongation,[12–15] although it is limited by the elastomer's stretchability and the stress concentration caused by the embedded rigid components.

Conformal contact, achieved by incorporating soft matter, is crucial for efficient heat transfer in thermoelectric devices. However, the performance of these devices can be significantly improved with the use of soft and stretchable functional materials and an optimized device structure for thermal management. From a materials perspective, employing stretchable thermal interface materials for contact surfaces,[3] reducing the thermal conductivity of the middle layer,[16,17] and precisely controlled layer dimensions[16] offer promising avenues to increase the performance of flexible and stretchable thermoelectric modules. Among thermally conductive materials suitable for stretchable

Y. Han, H. Tetik, M. H. Malakooti
Department of Mechanical Engineering
University of Washington
Seattle, WA 98195, USA
E-mail: malakoot@uw.edu
Y. Han, M. H. Malakooti
Institute for Nano-Engineered Systems
University of Washington
Seattle, WA 98195, USA
M. H. Malakooti
Department of Materials Science and Engineering
University of Washington
Seattle, WA 98195, USA
The ORCID identification number(s) for the author(s) of this article can be found under https://doi.org/10.1002/adma.202407073

DOI: 10.1002/adma.202407073

 

TEDs, liquid metal elastomer composites stand out for their simple fabrication process, tunable microstructures, low stiffness, and high conductivity.[18–23] This is because, unlike solid fillers, the liquid phase inclusions can soften the polymer or have a minimal stiffening effect based on the droplet size and choice of polymer matrix.[24] This ensures low softness for conformal contact with non-planar surfaces in TEDs. In addition, the high thermal conductivity of embedded LM particles (20–30 W $m^{-1}$ $K^{-1}$) facilitates heat transfer to the thermoelectric materials. One study demonstrated that employing liquid metal-embedded elastomer at the interface significantly enhances thermoelectric performance compared to pristine elastomer, marking the first application of LM composites in TEDs.[3] This multifunctional composite was later tailored to fabricate a stretchable thermoelectric generator (TEG) with a maximum strain of 60% and a power density of 86.6 μW $cm^{-2}$ at a temperature gradient of 60 °C.[25] However, efficient thermoelectric energy conversion at low-temperature gradients has yet to be attained, which is crucial for wearable TEGs and powering electronics from body heat at room temperature.

Despite significant advances and the rise of new applications for TEDs, such as shape memory actuation,[26] this class of stretchable electronics has not yet realized its full potential. This is primarily due to challenges related to low thermoelectric energy conversion, as well as issues with durability, robustness, and fabrication process. For instance, one study utilized a soft thermal interface with magnetically aligned silver-nickel heat conduction pathways for wearable thermoelectrics, achieving a power density of 418.6 μW $cm^{-2}$ at a temperature gradient of 40 °C.[27] However, despite successfully lighting LEDs using TED-integrated gloves attached to a hot kettle (≈70 °C), the device could not harvest enough energy from the temperature difference between the body and the surrounding environment for practical use. This can be attributed to the high fill factor of TE pellets at 26.6% which compromises the thermal management within the device as well as limited mechanical compliance and stretchability with failure strain at 20%. Furthermore, the subtractive fabrication process employed in the study hinders scalability and manufacturing flexibility. We recently addressed the fabrication bottleneck by 3D printing functional elastomer composites.[16] While the printed TEG showed a high power density of 649.9 μW $cm^{-2}$ at the temperature gradient of 60 °C, the harvested energy at low-temperature gradients is insufficient to power wearable electronics. This is primarily because of reduced thermoelectric energy conversion when the device reaches thermal equilibrium. These TEGs also demonstrated high mechanical robustness, enduring 15 000 stretching cycles at 30% strain without electrical or mechanical failure. However, the use of Sylgard 184 as the base polymer in the composites limits the flexibility of the printed TEDs, reducing their conformal contact and performance, especially in devices with greater thickness.

In this work, we report 3D printing of soft architectures for damage-tolerant thermoelectric devices, setting new performance records for energy harvesting while achieving exceptional conformability. This accomplishment stems from the successful integration of stretchable functional composites through 3D printing, the use of self-healing liquid metal interconnects, the incorporation of inorganic TE materials, and a deliberately designed device architecture for optimal thermoelectric energy conversion and preserved structural integrity (**Figure 1a**). The designed structure is first determined through multiphysics simulations, and the 3D printing of a liquid metal elastomer composite (LMEC) and a stretchable thermal insulator is subsequently employed to fabricate highly deformable TEDs for wearable applications with unique features, such as a stretchable heatsink (Figure 1b). To investigate the effect of the thermal insulation layer structure, the printed TEDs feature three distinct infill ratios (0%, 12%, and 100%) in the core layer, representing thermoelectrics with an interlayer gap, air pockets, and a densely filled layer, respectively.

While the low conductivity of the hollow microsphere elastomer composite (HMEC) in the thermal insulation layer is effective in concentrating heat flux in the TE legs, the presence of air pockets demonstrates higher voltage generation and does not compromise the device stretchability, as shown in Figure 1c. The results indicate that the soft-matter-engineered TEDs, featuring stretchable multifunctional materials and lightweight thermal insulation interlayers, can withstand up to 600% uniaxial strain before mechanical failure, with electrical interconnects maintaining connectivity up to 230% strain. Importantly, TEDs stretched close to 600% without experiencing mechanical failure and regained their electrical conductivity when returned to their unstrained condition. Additionally, these TEDs can restore their energy harvesting and active heating/cooling after being punctured multiple times with a sharp object. This is attributed to the use of liquid metal and its ability to recreate conductive pathways upon contact. Furthermore, the punctured devices can fully function after undergoing 2000 stretching cycles from 0% to 50% strain, enabled by the combined effect of the ultrasoft composites with enhanced toughness and self-healing interconnects.

These thermoelectric generators, featuring stretchable 3D structures, achieve a considerably high power density of 115.4 μW $cm^{-2}$ at a low-temperature difference (ΔT) of 10 °C. Once the device reaches thermal equilibrium after an initial ΔT of 10 °C, the power density decreases to 16.1 μW $cm^{-2}$. When considering normalized power density relative to the temperature gradient across the device and strain limit, our thermoelectric generators significantly outperform recent stretchable TEDs as depicted in Figure 1d and Figure S1 (Supporting Information).[16,17,25–42] Due to the use of various test setups in the literature to report the performance of stretchable TEGs, a detailed discussion on TED characterization (Figure S2, Supporting Information) and reported values (Table S1, Supporting Information) is provided in the Supporting Information. Regardless of these differences, a series of innovations in this study improve energy harvesting performance by 70% and incorporate damage tolerance, thus addressing previous challenges and making their applications feasible. This level of energy conversion can immediately power an LED upon contact with the body at ambient temperature, (Video S1, Supporting Information), as demonstrated for the first time. This milestone unlocks the potential of Macro-TEDs as a reliable power source for wearable electronics (Figure 1e).

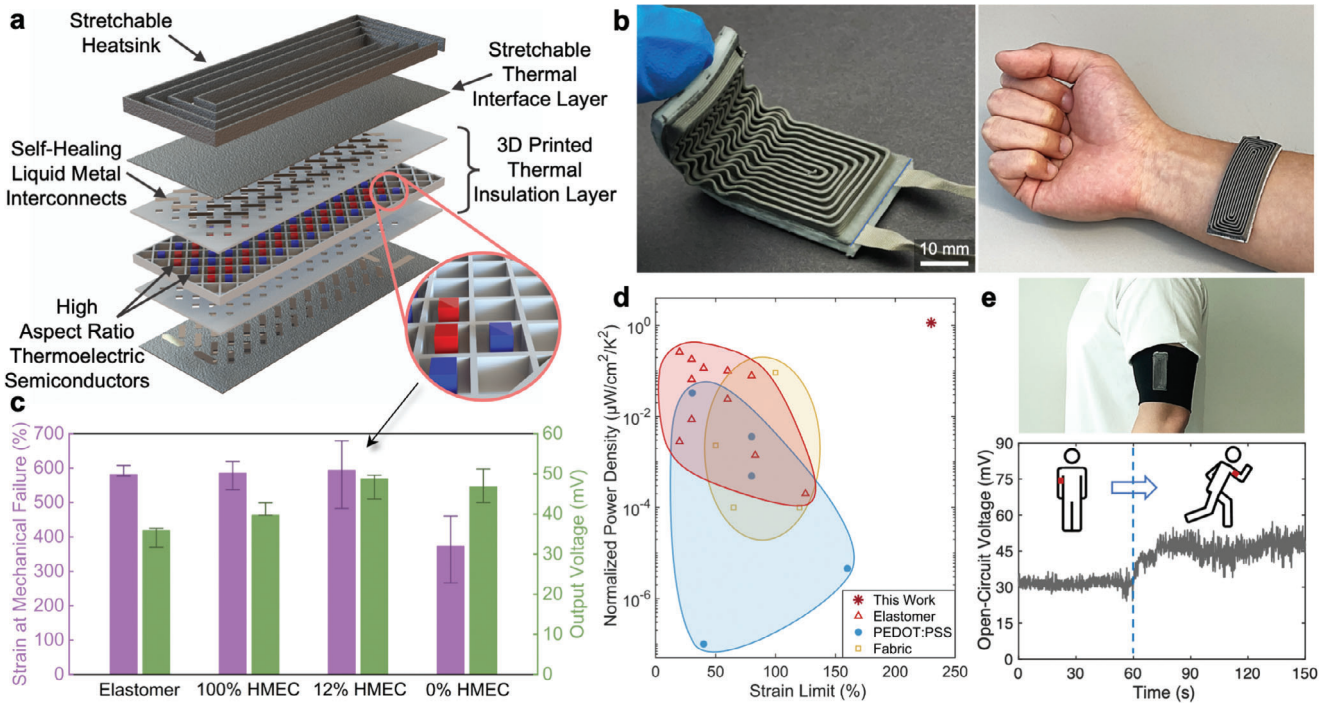


**Figure 1.** High-performance, stretchable thermoelectric device (TED) with 3D soft architectures. a) Schematic illustration of the device design and its multifunctional layers. b) Images of the TED when it is bent by a finger (left) and worn on the wrist (right). c) Comparison of stretchable TED tensile test specimens with respect to strain at mechanical failure and output voltage at equilibrium. d) Scattered plot for comparison of soft and stretchable TEDs. e) A wearable thermoelectric generator is worn on the upper arm with enhanced energy harvesting during running.

## 2. Results and Discussion

### 2.1. Functional Matter for Stretchable TED

To create 3D-structured stretchable thermoelectrics, we formulated two elastomer inks for printing the thermal interface and thermal insulation layers. The thermal interface material utilizes a composite of LM droplets (EGaIn: eutectic gallium-indium) and an ultra-stretchable silicone elastomer (Ecoflex 00–30),[19] with proven biocompatibility.[43] This LMEC, with a 50% volume fraction of EGaIn and an average particle size of 13.7 μm (Figure S3, Supporting Information), shows a relatively high thermal conductivity of ≈1.3 W m$^{-1}$ K$^{-1}$ (**Figure 2a**) without electrical conductivity. The selection of Ecoflex 00–30 as the polymer matrix is essential because its high elongation at break (>900% strain) enables device stretchability, and its low elastic modulus (68.9 kPa) prevents the formation of conductive pathways between LM particles at this scale.[44]

For the thermal barrier, we used the same base polymer to ensure robust layer bonding. This time, hollow thermoplastic microspheres (Expancel) are dispersed within the elastomer to reduce its thermal conductivity and weight. This HMEC separates the two thermally conductive layers at the top and bottom and provides structural support for the TE legs. Although the hollow microspheres have a low density of 0.0309 g cm$^{-3}$, they can be uniformly distributed in the elastomer at a 50% volume fraction (Figure S4, Supporting Information). The thermal conductivity of the HMEC is measured to be ≈0.1 W m$^{-1}$ K$^{-1}$ and its density is calculated to be 0.723 g cm$^{-3}$ which corresponds to a 32.4% reduction from the unfilled elastomer ($\rho_{\text{Ecoflex}}$ = 1.07 g cm$^{-3}$). Therefore, the HMEC is a lightweight soft matter that enhances heat management within the device by concentrating the heat flux to the TE pellets and reduces the TED's weight when used as a thermal insulation material in the core layer.

Thermoelectric semiconductors in TED play a key role by harnessing the Seebeck effect to generate electricity from temperature gradients,[45,46] or employing the Peltier effect for heating or cooling.[47] Bismuth telluride ($Bi_2Te_3$) stands out as the thermoelectric material of choice because of its advantageous combination of low thermal conductivity (1.2–1.6 W m$^{-1}$ K$^{-1}$), high electrical conductivity (850–1250 S cm$^{-1}$), and excellent Seebeck coefficient (200–235 μV K$^{-1}$), resulting in exceptional figures of merit ($zT$) and conversion efficiency at ambient temperatures.[48–50] Hence, inorganic p-type and n-type $Bi_2Te_3$ hold great promise for achieving high energy conversion in the device, while their brittleness and rigidity are mitigated by soft functional matter and liquid-phase electrodes. The hybrid-structured device leverages high $zT$ thermoelectric materials and offers excellent mechanical flexibility that is essential for conformal contact with non-planar surfaces (e.g., the human body) and effective heat conduction.

### 2.2. Enhanced Efficiency via Device Architecture

To maximize the energy conversion in stretchable thermoelectrics, the heat management within the TED must be optimized. We applied certain design principles and studied the device's performance through simulations and experiments.

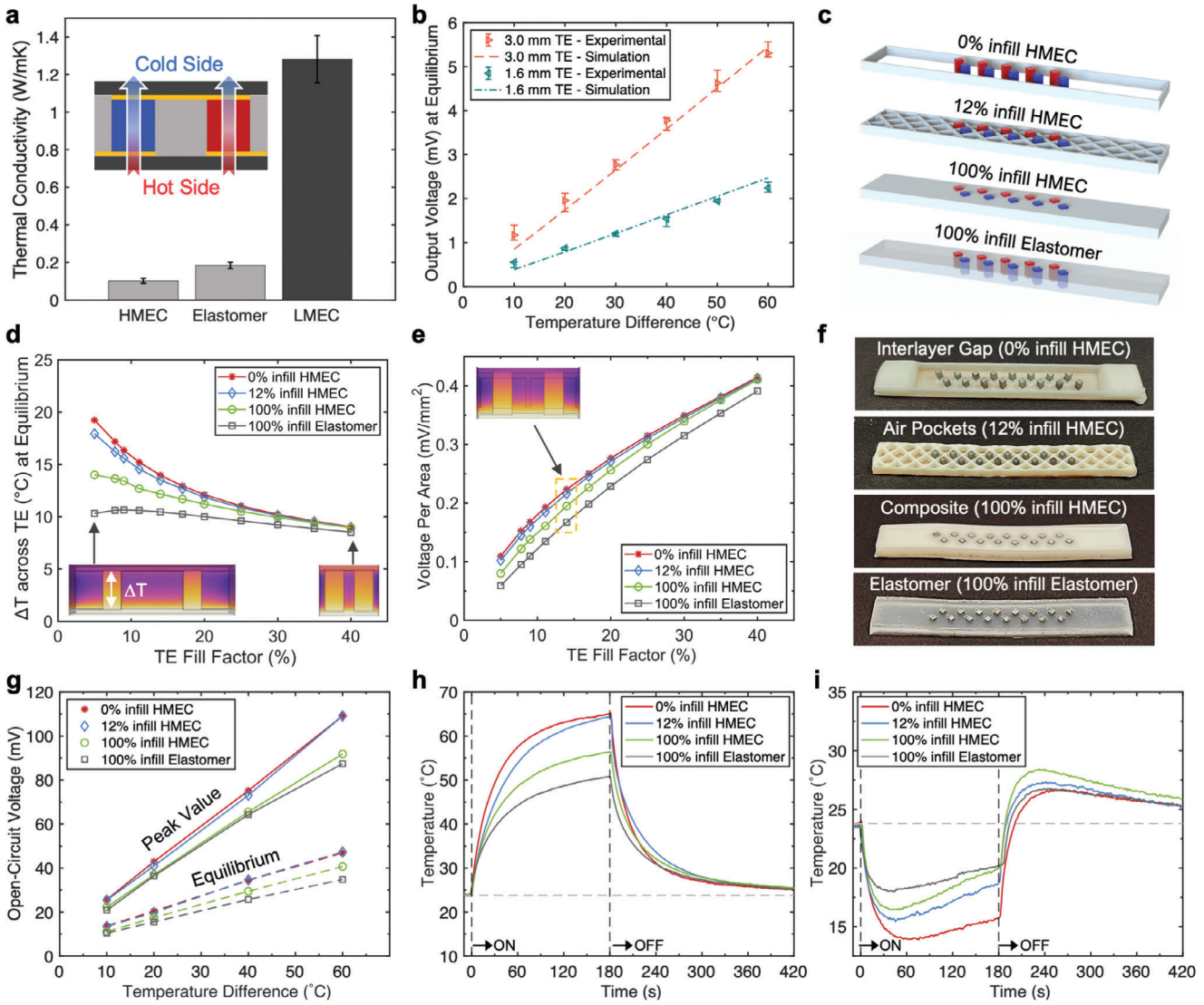


**Figure 2.** Enhanced energy conversion through soft-matter engineering: a) Thermal conductivities of the materials in the core layer (HMEC and unmodified elastomer) and thermal interface layers (LMEC). b) Simulation and experimental data for a pair of low and high-aspect ratio TE legs in a densely filled HMEC core layer. c) Schematics of four different designs of the core layer. d) The temperature gradient across TE pellets at thermal equilibrium from the simulation of a single pair of TE pellets with four different core layers at $\Delta T = 60$ °C. Inset: Cross-section images of 5% and 40% TE fill factors with the simulated temperature profile. e) Output voltage at thermal equilibrium normalized by area from the simulation of a single pair of TE pellets. Inset: A cross-section image of a 14.2% TE fill factor with the simulated temperature profile. f) Photographs of the four different core layer architectures. g) Measured peak and steady-state values of the open-circuit voltage with different initial temperature gradients. h) Measured surface temperature of TEDs in active heating mode over time. The power was switched off after 3 min. i) Measured surface temperature of TEDs in active cooling mode for 3 min. Parasitic heating is observed after the current is switched off.

Increasing the height of TE legs is an effective strategy to increase the temperature gradient across the device as the distance between the hot and cold sides has increased. Figure 2b shows the experimental and simulated open-circuit voltage ($V_{OC}$) at thermal equilibrium for a pair of TE legs with two distinct aspect ratios: $1.4 \times 1.4 \times 1.6$ and $1.4 \times 1.4 \times 3.0$ mm$^3$. The simulation result is validated experimentally with a normalized output voltage of TED samples, demonstrating excellent agreement in $V_{OC}$ of various temperature gradients. For the same cross-sectional area, the $Bi_2Te_3$ pair with 3.0 mm in height represents the high aspect ratio TE legs, which in turn produces a higher output voltage. Moreover, while both cases show a linear increase in output voltage with increasing the hot side temperature with respect to the ambient temperature, the high aspect ratio TE legs show a more rapid increase. Therefore, we have chosen to utilize the high aspect ratio TE due to their enhanced and consistent energy conversion, and study other structural facets of the device.

Other factors that significantly affect heat management and energy conversion in TED are the thermal and geometrical properties of the insulation layer as well as the area fraction of the TE legs. 3D printing of soft functional matter allows design freedom with the possibility of improved performance and

integration of unique features such as 3D stretchable heatsinks for TED, as we demonstrated in our previous study.[16] We extend this capability by leveraging 3D printing to create 3D soft architectures with low thermal conductivity in the core layer of the TED. We studied four different structures (Figure 2c) through simulation and experiment. Based on the 3D printing infill percentage and print materials, we have classified four distinct designs as follows: TED with interlayer gap (0% infill HMEC), featuring no material deposition between the top and bottom surfaces except for a shell around the device; TED with air pockets (12% infill HMEC), using a simple 12% infill density pattern to print HMEC between TE legs for structural support; the third design involves densely filled HMEC (100% infill HMEC), HMEC fully covers the space between thermal interface layers; and the fourth design comprises densely filled elastomer (100% infill Elastomer), with the base elastomer fully covering the space between thermal interface layers and serving as the common device structure for elastomer-based thermoelectric generators.

The characterization method for TEDs should be established before investigating the effect of device geometric parameters. In the context of wearable applications, human skin acts as a deformable heat source, with heat primarily dissipating to the ambient environment through natural convection. Given these conditions, we chose the "One Side Heat Conduction" method (Figure S2, Supporting Information). To characterize the energy harvesting performance of the TED, the device is placed on a heat source so that heat is applied from one side and dissipates on the opposite side through convection. In this measurement, the output voltage peaks initially and then gradually reduces until it stabilizes when the TE legs reach thermal equilibrium. Using this method at higher temperature gradients is challenging because of the device's relatively small thickness and the high thermal energy supplied by the heat sources. We focus on the response at equilibrium because of its higher practical relevance. This approach indicates the device's ability to consistently generate power across a wider range of temperatures on the hot side without the need for active heating and cooling mechanisms on each side.

To study each of the four designs in Figure 2c at thermal equilibrium, we employ multiphysics finite element modeling to evaluate the combined effects of the packing density of the rigid TE semiconductors (TE fill factor) and the core layer's material and structure. The applied boundary conditions and input parameters used in the finite element model are detailed in Figure S5 and Table S2 (Supporting Information). The simulation results indicate a strong influence of both the TE fill factor and the core layer materials and design on the temperature gradient ($\Delta T$) across a pair of TE legs, as depicted in Figure 2d.

To maximize the $\Delta T$ across the embedded TE pellets (Figure 2d-inset), which directly increases the output voltage, it is essential to minimize the overall thermal conductivity of the core layer. This overall conductivity is influenced by several factors, including the design type, the thermal properties of the materials, and the TE fill factor, which represents the fraction of the total available area or volume occupied by the active TE phase (Figure S6, Supporting Information). For example, TEDs densely filled with HMEC are more effective than those using unfilled elastomer due to the lower thermal conductivity of the HMEC (Figure 2a), confirming that a promising approach to decreasing the effective thermal conductivity of the core layer is to employ a composite with lower thermal conductivity in this layer. In addition, employing 3D structures (TEDs with air pockets) or eliminating this layer (TEDs with an interlayer gap) results in a greater $\Delta T$ across the TE phase, which in turn produces higher voltage and power under the same heating conditions. This is because the low thermal conductivity of air prevents heat conduction from inactive phases, concentrating the heat flux onto the semiconductors. However, as the fill factor increases, the simulated $\Delta T$ decreases and eventually converges for all different designs and materials used in the core layer. This occurs at high TE filler factors because the overall thermal conductivity of the core layer increases since it is mainly occupied by the TE material (Figure 2d-inset), which, in this study, is bismuth telluride with higher conductivity compared to air, base elastomer, and HMEC.

It is important to highlight that a higher TE fill factor, which corresponds to a greater number of TE legs arranged in a unit area, leads to an increased normalized $V_{OC}$, as shown in Figure 2e. Despite a smaller temperature gradient across the TE phase, the greater TE content within a given space allows for more efficient energy conversion, resulting in a continuous increase in normalized output voltage as the fill factor increases. Nonetheless, the simulation results presented in Figure 2e suggest that despite the differences in TE fill factor, TEDs with interlayer gap (0% infill HMEC) and TEDs with air pockets (12% infill HMEC) show similar output voltage per area when reaching a steady-state condition, making these findings relevant for continuous power generation and practical applications.

For experimental validation and design comparison, we fabricated TED samples with the four distinct core layers as shown in Figure 2f. An infill percentage of 12% was chosen first based on the print resolution achievable with direct ink writing, and a TE fill factor of 14.2% was selected due to its substantial output voltage while maintaining noticeable differences in the energy harvesting performance between different core layer structures. Also, the fluidity and capillary force of uncured inks prohibited higher packing of TE pellets. Figure S7 (Supporting Information) illustrates the layer-by-layer fabrication process of the devices ($70 \times 10 \times 4$ mm$^3$ with 16 TE pellets) and includes photos of the 12% infill HMEC sample with visible regions that indicate the air pockets with trapped air, which serves to concentrate the heat flux onto the TE pellets, enhancing energy conversion at equilibrium.

The $V_{OC}$ of four different TE specimens is measured at initial temperature gradients ranging from 10 to 60 °C for 150 s to comprehensively understand the voltage response upon contact with the heat source. The voltage generated from TEDs follows a similar trend: it initially exhibits a peak response, then it decreases over time until it stabilizes at equilibrium (Figure S8, Supporting Information). However, the $V_{OC}$ from low infill cases (0% and 12% infill HMEC) exhibits significantly higher values than the other two TEDs with densely filled core layers, confirming the improved thermal management within the device and enhanced energy harvesting performance. Figure 2g provides a summary of $V_{OC}$, both peak and steady-state values, in relation to the temperature gradient. The results indicate an excellent alignment with the simulation data. TEDs with 0% and 12% infill HMEC show nearly identical responses. This similarity can be attributed to the

structural differences between these TEDs. While TED with air pockets has extra material in the core later that allows heat transfer, it has robust support to the top layer. However, TED without any support material in the core layer can easily bend under its own weight, resulting in a reduction of the distance between the hot and cold sides of the device. This structural contrast clarifies the similarity in their responses. Furthermore, Figure 2g illustrates the impact of core layer material and structure modifications. Replacing the base elastomer with a low thermal conductivity composite (HMEC) yields a substantial 13% increase in $V_{OC}$ while an additional improvement of 14% is achieved by printing HMEC with a 2D lattice structure (i.e., air pockets).

In addition to their energy harvesting functionality, stretchable thermoelectric devices can be employed for active heating and cooling applications when supplied with electricity. Each of the four designs is anticipated to yield a unique temperature profile. Figure 2h–i shows temperature changes in TED specimens for on-demand heat and cooling when placed on a polystyrene substrate (Video S2, Supporting Information). Under the influence of an electric field, TE pellets create a temperature gradient, and the resulting heat flux is transferred to the thermal interface layers, causing the device's surface to either heat up or cool down. It is postulated that the combination of Joule heating and the Peltier effect is responsible for the heating function, while only the Peltier effect brings the temperature down on the cold side of the TED.[47] Figure 2h demonstrates the significantly enhanced active heating performance because of the 3D soft architecture in the core layer when comparing the four TEDs under a 1 A direct current. As expected, the TED with 100% infill Elastomer exhibits the least temperature increment with a slow response rate due to its less efficient thermal management. In contrast, the TEDs with 0% and 12% infill HMEC show similar and considerably improved responses, indicating their promising performance in active heating applications. Similarly for active cooling, Figure 2i highlights the effective reduction and control of temperature when there is less material in the core layer. This is because the supporting structure allows heat conduction between the thermal interface materials, decreasing the thermal management capability compared to the interlayer gap. Furthermore, the lower infill in the core layer suppresses parasitic thermal residue from spreading to the opposite side once the power is turned off. These thermoelectrical responses suggest the importance of TED's architecture to align with its intended purpose, whether it is energy harvesting or temperature modulation.

### 2.3. Electromechanical Robustness and Electrical Self-Healing

Ensuring robustness against large deformation and external damage is essential for the practical applications of TEDs. **Figure** 3a shows the flexibility of our TEDs, capable of simply bending at two points, even with embedded 3.0 mm rigid semiconductors. To systematically study the stretchability of the designed TEDs, we first conducted tensile tests on the soft elastomer composites to characterize the mechanics of each layer within the device. Figure S9 (Supporting Information) shows the tensile specimens comprising HMEC, LMEC, and printed HMEC with 12% infill, along with the obtained stress-strain plots that show the material's elasticity. The results show that the thermal interface material, LMEC, is highly stretchable with an average failure strain of 979% while the thermal insulation material, HMEC, is slightly stiffer with a reduced failure strain of 768%. This difference comes from embedding liquid inclusions versus solid, yet hollow microspheres. When testing specimens with 12% infill HMEC in the reduced section, the failure strain remains reasonably high at 710%. These material properties imply that the TEDs are expected to show a high level of stretchability regardless of the embedded TE pellets and layered structure.

Tensile tests on the four types of TEDs demonstrate remarkable mechanical strain at failure of nearly 600%, except for the device with interlayer gap (Figure 3b). This level of extensibility comes from the intrinsic properties of the base elastomer and the seamless fabrication process, while the TE pellets in the core layer cause stress concentration in the soft structure, restricting its stretchability, as shown in Figure S10 (Supporting Information). Since the TED with interlayer gap lacks materials in the core layer to provide structural support for the thermal interface layers and TE pellets, this design tends to experience premature failure under tension. In Figure 3c, a comparison of device stiffness reveals that the TED with 100% Elastomer shows the lowest stiffness, while the device with 100% HMEC exhibits the highest average stiffness due to HMEC's greater stiffness compared to unmodified elastomer and thermal interface layers. However, reducing the infill percentage mitigates the stiffening effect of the HMEC on the device. This result indicates that TEDs with air pockets are mechanically robust and capable of achieving conformal contact with non-planar surfaces for effective thermoelectric energy conversion.

Room-temperature liquid metal electrodes and the elastomer encapsulation provide TED with a stable electrical response under large deformations. Cyclic loading tests for each TE tensile specimen are conducted to study electromechanical robustness over an extended period, as shown in Figure 3d. A 50% strain was chosen, as it is comparable to human skin tolerance and exceeds the commonly used design criterion for wearable electronics.[51,52] The excellent electrical conductivity ($3.4 \times 10^6$ S m$^{-1}$) and fluidity of liquid metal interconnects result in a negligible change in the internal resistance of the TEDs over 2000 cycles. Examining the resistance changes when the TED with air pockets is stretched to twice its original length reveals that the electrical connections in TED remain intact at 100% strain, with only a minor increase in resistance by 0.14 Ω (Figure S11, Supporting Information). This stable electrical response, combined with the thermoelectric performance and mechanical strength of the four different device architectures, leads to the conclusion that the design featuring high aspect ratio TE legs with air pockets in the core layer is suitable for wearables. To be more specific, this design yields a 29% higher voltage at thermal equilibrium compared to the control sample, TED with 100% infill Elastomer. Furthermore, it achieved a significant 79.7% weight reduction in the core layer compared to the control sample by replacing the dense elastomer layer with a 3D soft and stretchable architecture, all the while leveraging the benefits of mechanical and thermal management.

Besides stable electromechanical response, the energy harvesting performance of the TED with air pockets is studied under

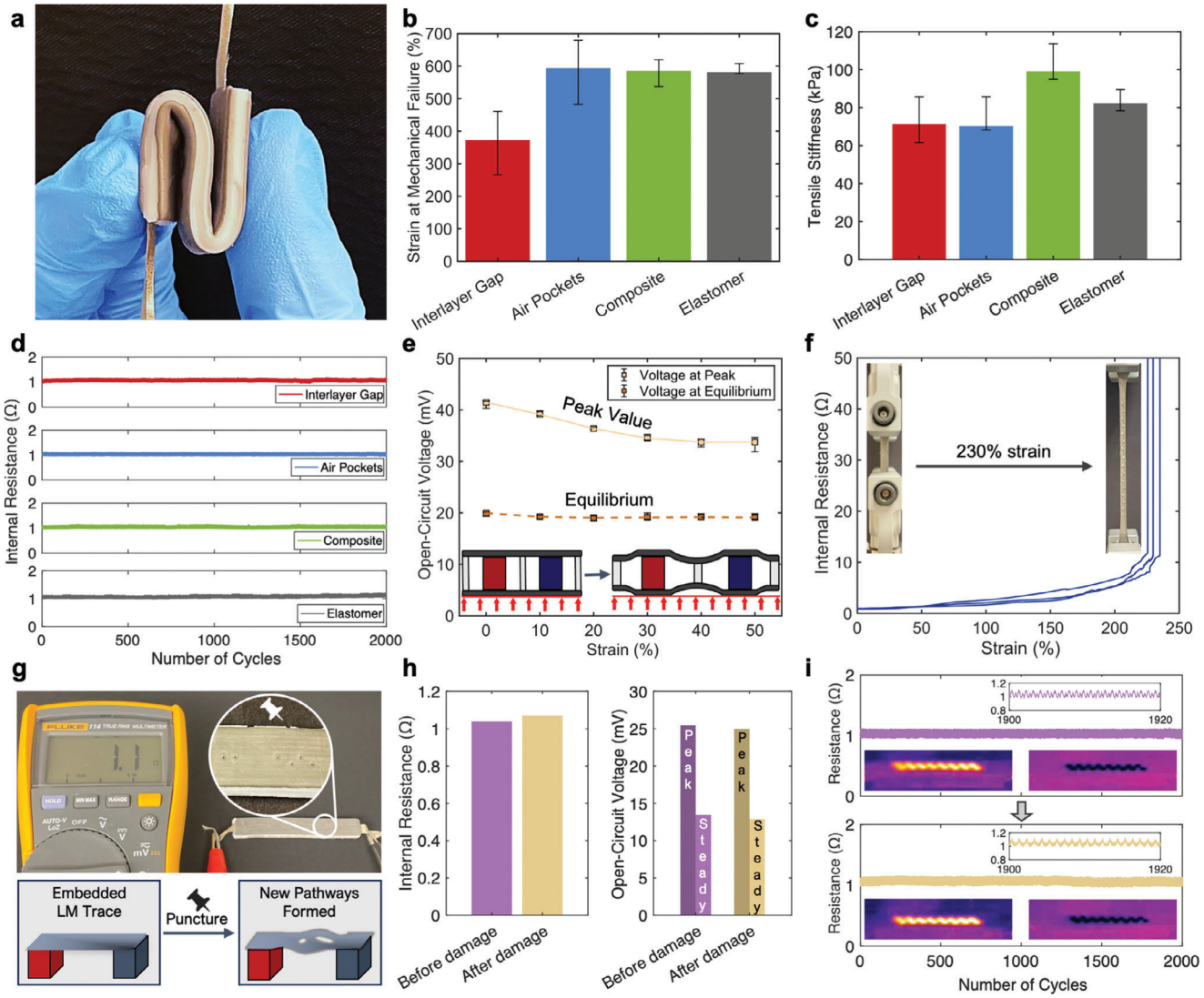


**Figure 3.** Electromechanical response and self-healing: a) Photograph of folded TED with air pockets. b) Maximum strain at mechanical failure and c) Measured stiffness of four different designs under uniaxial tension. d) Measured internal resistances of four different TE tensile specimens over 2000 cycles of 0 to 50% uniaxial strain. e) Measured open circuit voltages of air pocket TE tensile specimen under 0 to 50% uniaxial strain at the temperature gradient of 20 °C. Inset: schematics of TED cross-section when uniaxially strained. f) Measured internal resistances of air pocket TE tensile specimen with electrical disconnection at 230% strain on average. g) A photograph of the TE specimen after being punctured by a pushpin (top) and the schematic of electrical self-healing (bottom). h) Measured internal resistance and open-circuit voltage responses at peak and thermal equilibrium of the TED tensile specimen before and after being pierced by a push pin. i) Measured internal resistances before and after being punctured for over 2000 stretching cycles of 50% uniaxial strain. Inset: IR images of active heating (left) and cooling (right) before and after damage.

tensile strain to ensure its capability to generate power when stretched. Figure 3e shows the measured $V_{OC}$ at $\Delta T = 20$ °C as a function of applied uniaxial strain, varying from 0% to 50%. Although the peak value slightly decreases with higher strain, there are negligible variations in output voltage when the device reaches thermal equilibrium. This is because initially, the thermal interface deforms nonuniformly due to the embedded rigid TE legs, resulting in less conformal contact with the hot surface (Figure 3e-inset) and reduced heat flux in the TE. However, the LMEC thermal interface effectively transfers heat over time, resulting in a constant voltage across the strain range from 0% to 50%.

The excellent stretchability of thermoelectric devices with a 3D soft architecture is also evident from their stable internal resistance up to a strain level of 230%, as shown in Figure 3f. This indicates that the device remains fully operational until it experiences exceptionally high tensile strain. Under such large deformations, the rigid TE pellets can disrupt the connection between the liquid phase conductive traces, causing sudden electrical failure. Since these devices do not mechanically fail up to 600% strain, the once electrically failed TE specimens recover their functionality when returned to their initial state at 0% strain. This is because of the elastic deformation and resilience of the stretchable 3D architecture, which realigns the LM interconnects when the strain is

removed, and the fluidity of the LM, which allows it to reconnect and regain electrical conductivity upon contact with other segments of the LM traces.

Alongside extreme stretchability, LM interconnects equip the TEDs with electrical self-healing during operation. Figure 3g and Video S3 (Supporting Information) illustrate the device's ability to self-repair and maintain its functionality, even after being punctured multiple times with a sharp object. We demonstrate this autonomous self-healing feature by comparing the internal resistance and open-circuit voltage of the TED before and after damage. As depicted in Figure 3h, the resistance and $V_{OC}$ show negligible change in both peak and steady-state response after the device is punctured with a push pin. The self-healing behavior of the LM circuitry is attributed to the formation of new conductive pathways in the EGaIn interconnects and the immediate formation of the gallium oxide layer upon each piercing or cut.[53–56] Furthermore, the soft elastomer composites in TED keep the device physically intact, preventing premature mechanical failure. To further highlight this unique capability, we examined the electromechanical response of the TED with air pockets before and after damage. Figure 3i shows the measured device resistance during cyclic mechanical loading from 0 to 50% strain for 2000 cycles. The damaged device exhibits virtually identical electrical responses with no apparent signs of mechanical or electrical failure. The demonstrated high level of damage tolerance and stable electromechanical behavior suggests not only consistent thermoelectric energy conversion but also robust temperature modulation of our TEDs even after the piercing. To illustrate this, we analyzed TED's heating and cooling performance by comparing the IR photos before and after damage in Figure 3h-inset. Moreover, the punctures have no impact on the heating and cooling rates or TED's surface temperatures, as evident in Videos S4 and S5 (Supporting Information). This self-repair behavior is due to the reconfigured LM pathways connecting the TE legs, confirming that these thermoelectrics can also maintain their functionality as a temperature modulator when damaged. The mechanical robustness and consistent high performance of our TEDs, even under severe conditions, lay a foundation for their macro-scale implementation and practical applications.

### 2.4. Soft and Stretchable Macro-TED

TEDs must cover an optimal area to harvest considerable amounts of energy at low temperature gradients or effectively heat up or cool down surfaces on demand, enabling applications such as powering sensors or providing localized thermal comfort. To address this need, we leveraged the insights from our systematic study and fabricated Macro-TEDs with air pockets in the core layer and 48 pairs of high aspect ratio TE semiconductors (**Figure** 4a). The maximum output voltage and power are measured in the range of 115.7–648.5 mV (Figure 4b and Figure S12, Supporting Information) and 1.4–39.2 mW (Figure S13, Supporting Information), respectively, as we varied the temperature across the thermoelectric generator from 10 to 60 °C. After reaching thermal equilibrium, the $V_{OC}$ reduces to ≈30% of its peak value (Figure S12, Supporting Information) and the generated power stabilizes at 0.12 and 3.19 mW for the initial temperature gradients of 10 and 60 °C as shown in Figure 4c. For all different temperature ranges, the optimal power is obtained when the external load resistor is 2 Ω, which is relatively close to the TED's internal resistance at 2.7 Ω. With the "One Side Heat Conduction" method, we measured power densities up to 3 mW $cm^{-2}$ at $\Delta T$ = 60 °C when considering the peak value in the signal (Figure S13, Supporting Information). However, for practical purposes, we consider the power density at equilibrium, which ranges from 9.3 to 241.8 μW $cm^{-2}$ based on the initial temperature difference. This power-harvesting capability, especially at low-temperature gradients, makes our stretchable thermoelectric generator an ideal candidate for emerging applications, such as self-powered wearable electronics.

To further enhance thermoelectric energy conversion under steady-state conditions, we employed 3D printing to create a soft and stretchable heatsink using the same liquid metal composite on one side of the Macro-TED. As illustrated in Figure 4d, the heatsink effortlessly bends and stretches along with the device due to its inherent compliance. This innovative heatsink, featuring a 3D soft architecture, is anticipated to improve heat management within the device, particularly in the context of convection boundary conditions. As shown in Figure 4e, the power density at thermal equilibrium is significantly increased from 9.3 μW $cm^{-2}$ to 16.1 μW $cm^{-2}$ at the low-temperature gradient of 10 °C, and from 241.8 to 358.5 μW $cm^{-2}$ at $\Delta T$ = 60 °C, respectively, by printing the soft 3D structured heatsink. Alongside power measurements, we studied changes in $V_{OC}$ over time, as shown in Figure 4f. The integrated heatsink increases TED's output voltage at equilibrium from 190.7 to 231.5 mV at $\Delta T$ = 60 °C. However, the heatsink is expected to be more effective under airflow conditions. Under simulated "light breeze" conditions (i.e., wind speed of 2.5 m $s^{-1}$), the TED exhibits a higher harvested voltage with faster convergency, while maintaining similar peak values. Under this forced air convection, $V_{OC}$ at steady-state condition increases from 341.9 to 388.5 mV with the stretchable heat dissipator. Similar trends are observed for $V_{OC}$ under different temperature gradients, as shown in Figure 4g and Figure S14 (Supporting Information). This data indicates the effectiveness of the 3D heatsink, resulting in a 32.2% increase in $V_{OC}$ without any airflow and an additional 17.5% increase after enhancing the output voltage through forced air convection.

Excluding the performance enhancements achieved under light breeze conditions, which may not be applicable in certain working environments, our soft-matter-engineered thermoelectric generator demonstrates an overall 70% increase in output voltage. This improvement is attributed to the thermal insulation material (13%), core layer architecture (14%), and deformable heatsink (32%). To showcase the collective impact of employing 3D soft architecture in TEDs, we utilized the generated power to charge a coin cell battery, comparing it with a conventional flexible TED as the control specimen. Figure 4h shows the measured voltages of the battery during charging with an initial $\Delta T$ of 60 °C. The TED with 3D soft architectures exhibits a faster charging rate compared to the reference device which has an unfilled elastomer and low aspect ratio TE legs in the core layer and lacks the 3D heatsink. This result indicates the promising application of high-performance stretchable thermoelectrics in self-sustainable electronics.

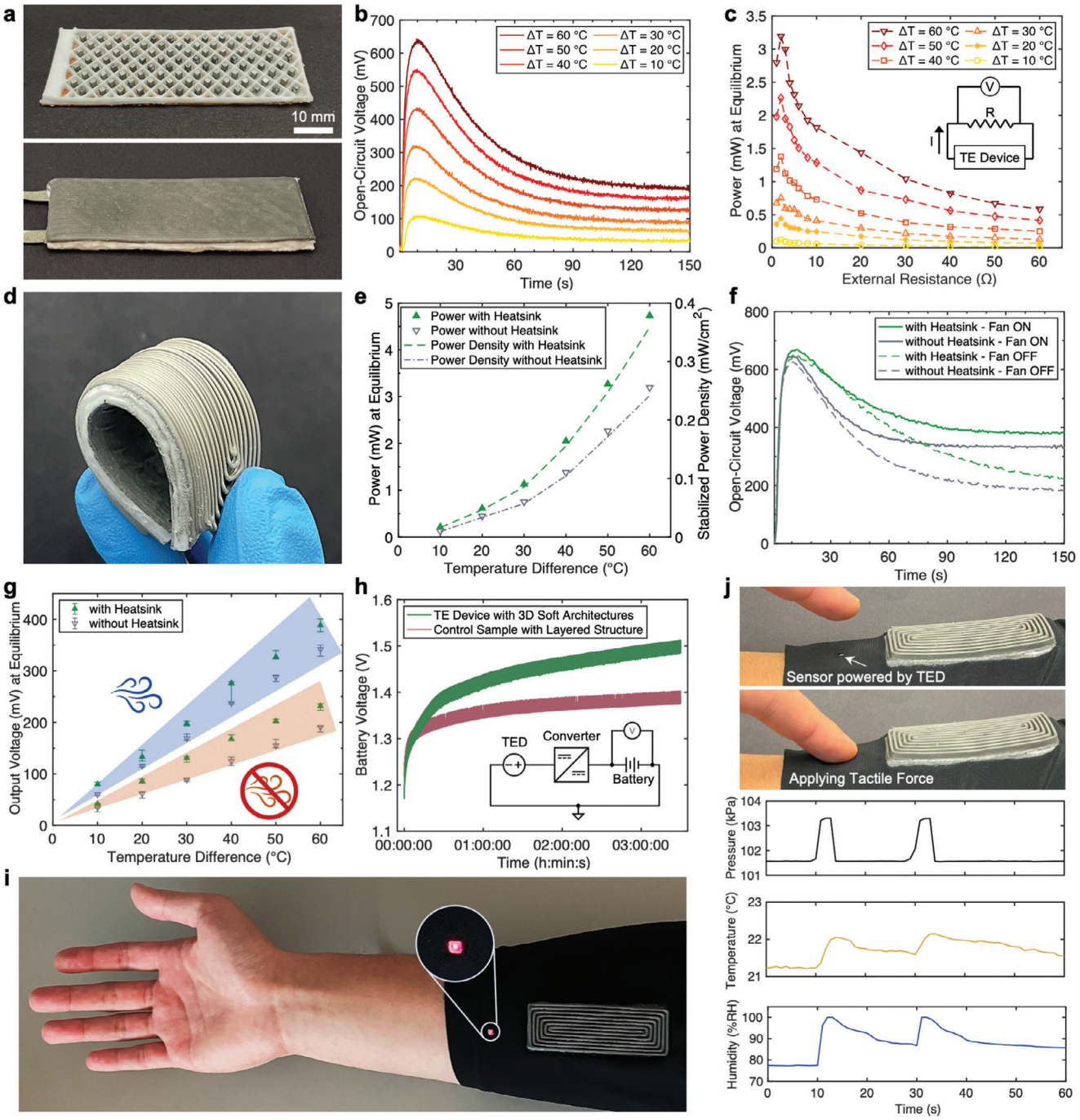


**Figure 4.** Macro-TED with the 3D soft architecture for higher energy harvesting performance and applications. a) Photographs of Macro-TED with 12% infill core layer and a dimension of 60 × 22 × 4 mm$^3$. b) Measured open-circuit voltage of Macro-TED at ΔT = 10 – 60 °C with respect to time. c) Measured power delivered from TED to load resistor at thermal equilibrium at ΔT = 10 – 60 °C with respect to the resistance. d) A photograph of Macro-TED with a stretchable heatsink being bent, showing its superior flexibility. e) Measured power and power density of the Macro-TED at thermal equilibrium with and without the stretchable heatsink with respect to the temperature gradient. f) Measured open-circuit voltage of Macro-TED with and without the heatsink and forced air convection as a function of time at ΔT = 60 °C. g) Open-circuit voltage at thermal equilibrium with and without the heatsink and forced air convection as a function of the temperature gradient. h) Measured battery voltage charged by TEDs with and without the 3D soft architecture at ΔT = 60 °C. An inset schematic shows the battery charging circuit with a boost converter. i) A photograph of an LED powered by harvested energy from body heat at room temperature (24 °C). j) Photographs that show sensors powered by TED being touched with a finger for wearable applications (top). Measured pressure, temperature, and humidity from the sensors powered by TED with respect to time (bottom).

### 2.5. Self-Powered Wearable Electronics

The most enabling feature of stretchable TEDs is their ability to conformally contact with non-planar surfaces, making them suitable for wearable electronics. Effective energy conversion at low-temperature gradients is also essential for realizing their full potential in wearable technology. Having addressed these two major bottlenecks, we demonstrate that our TEDs can be worn on the body to directly power LEDs and sensors. Figure 4i and Video S1 (Supporting Information) show that the TED illuminates an LED the moment it is placed on the forearm at room temperature. The temperature gradient between the forearm (34 °C) and the ambient temperature (24 °C) is only 10 °C, yet it is sufficient to power the LED due to the TED's enhanced performance. Importantly, this thermoelectric generator outperforms previously reported wearable thermoelectrics using three commercial TEGs in series with LMEC thermal interface materials,[3] as it requires only about a third of the temperature gradient and covers a much smaller surface area of the forearm. Thus, our stretchable TEDs exhibit remarkable performance, efficiently harnessing body heat for immediate LED activation, indicating their potential as a viable power source for wearables.

Moreover, we utilized our wearable thermoelectric generator to power two off-the-shelf sensors, facilitating dual sensing capabilities—one for pressure and temperature sensing and another for temperature and humidity sensing (Figure 4j and Video S6, Supporting Information). Both the thermoelectric device and the sensors are seamlessly integrated into a textile and worn on the forearm. The data indicate an instantaneous response of measured pressure and humidity to applied tactile force on the respective sensors and consistent values are measured upon repeated touches. The recorded high humidity and low temperature are due to the cold and rainy weather conditions during the experiment. This outcome demonstrates the advancements toward self-powered electronics, as TED eliminates the need for batteries and the associated inconvenience of replacement or recharging.

## 3. Conclusion

We have reported a soft and stretchable thermoelectric device distinguished by its unprecedented energy density and physical robustness, making it well-suited for emerging applications such as wearable and self-sustainable electronics. Employing multiphysics modeling, we analyzed various device architectures with the aim of sustaining a prolonged temperature gradient across the embedded TE semiconductors. Our experimental validations confirmed the effectiveness of the TED with air pockets and a supporting structure made from insulating elastomer composites at the core layer. This specific device architecture with tailored multifunctional composites not only showed high thermoelectric energy conversion but also exhibited significant structural integrity, withstanding stretching up to 230% strain before experiencing electrical failure.

Extending our analysis to the damage tolerance of these stretchable TEDs, our findings revealed no perceptible changes in electrical resistance, electromechanical response, energy harvesting performance, and active heating and cooling functionalities before and after being punctured with a sharp object. The electrical self-healing and stability demonstrated in the damaged device, even under 50% strain for over 2000 cycles, can be attributed to the incorporation of liquid metal conductors and the utilization of ultra-soft elastomer composites in these TEDs.

Furthermore, we showcased the scalability of our design and additive manufacturing process through the fabrication of a "Macro-TED" composed of 96 rigid TE pellets. Additionally, we printed a soft 3D architecture directly on the TED, serving as a stretchable heatsink to enhance the device's internal heat flux management. This Macro-TED, equipped with the heatsink, exhibited a power density peaking at 115.4 μW $cm^{-2}$, which stabilized at 16.1 μW $cm^{-2}$ under a low-temperature gradient of 10 °C. While our data confirmed the further improvement of thermoelectric energy conversion under forced air convection, we successfully demonstrated the capability of our TEDs to power electronics when worn on the body at an ambient temperature of 24 °C, eliminating the need for additional energy storage devices. These results and demonstrations highlight the potential of our high-performance, damage-tolerant, and stretchable thermoelectric devices in emerging applications such as wearable electronics, soft robotics, and self-sustainable intelligent systems.

## 4. Experimental Section

*EGaIn Synthesis*: Eutectic gallium–indium (EGaIn) was prepared by alloying gallium (99.99% purity, Luciteria) and indium (99.995% purity, Luciteria). Gallium was melted in the oven (Heratherm OGS60, Thermo Scientific) at 90 °C for 3 h. The liquid-state gallium was transferred to the glass jar and the indium was submerged into the gallium with the ratio of 75 wt% Ga and 25 wt% In. The jar was placed on a hot plate stirrer (Fisherbrand Isotemp) at 200 °C overnight to synthesize EGaIn.

*Thermal Interface Ink Formulation*: Ecoflex 00–30 (Smooth-On) and EGaIn were used to make LMEC ink for thermal interface printing. Ecoflex part A was poured into a 20 mL plastic cup and EGaIn was added drop-by-drop into the cup with a 1:1 volume ratio. The composite was mixed for 30 min at 600 RPM with an immersion mixer (Caframo, BDC250). Similarly, Ecoflex part B was poured into another plastic cup and EGaIn was added and mixed in the same manner. In this composite with Ecoflex part B, Slo-jo (Smooth-On) was added with a weight fraction of 4% of the total Ecoflex to prolong the pot life of the final ink. The two LMEC inks with different Ecoflex parts were transferred to another cup and shear mixed for 1 min at 2500 RPM using a planetary shear mixer (FlackTek SpeedMixer, DAC 150.1 FVZ-K) before being printed.

*Heatsink Ink Formulation*: Like the thermal interface ink, Ecoflex 00–30 and EGaIn are utilized for heatsink ink formulation. Ecoflex part A was poured into a 20 mL plastic cup and mixed for 30 min and 600 RPM by the immersion mixer. At the start of the mixing, EGaIn was added drop-by-drop to the plastic cup using the syringe until the EGaIn took 50%$V_f$ of the total volume of the mixture. In the same way, Ecoflex part B and EGaIn were immersion mixed in the different 20 mL plastic cups. Slo-jo was added to this cup with a weight fraction of 1% of the total Ecoflex. The two inks were transferred to another cup and shear mixed for 1 min at 2500 RPM in the shear mixer before transferring the heatsink ink to the syringe for printing.

*Thermal Insulation Layer Ink Formulation*: In a 20 mL plastic cup filled with part A of Ecoflex 00–30, Expancel (920 DE 80 d30; Nouryon) was added with the 50%$V_f$ based on the volume of the Ecoflex in the cup. THI-VEX (Smooth-On) was also added 2% wt of the Ecoflex part A in the cup to increase the viscosity while printing the ink. In a different 20 mL plastic cup, Ecoflex part B and Expancel were mixed with the same amount and ratio. In this cup, Slo-jo was added 2% wt of the Ecoflex part B. The two separate plastic cups were shear mixed using a planetary shear mixer (FlackTek SpeedMixer, DAC 150.1 FVZ-K) for 1 min and 2500 RPM. These

two inks were transferred to another cup and shear mixed for 1 min and 2500 RPM before printing the heat insulation layer architecture.

*Thermal Conductivity Measurement*: Thermal conductivities of multifunctional elastomer composites were measured by the transient hot wire method. A 25 mm-diameter platinum wire was soldered at each end to stranded copper wire and encapsulated within the elastomer composites. The composites were cast in an acrylic mold with a dimension of 70 × 10 × 4 $mm^3$ to cure them. The cured elastomer composites with the platinum wire were connected to a source meter (Keithley 2450), and the voltage was measured at 100 mA current for 0.9 s. Using nonlinear fitting, the thermal conductivity of each composite was calculated based on the input current, measured voltage, and the length of the platinum wire.

*Energy Harvesting Performance Measurement*: A hot plate stirrer (Fisherbrand Isotemp) was used as a heat source. The temperature of the surface of the hot plate and TEDs were measured with an IR thermometer (Fluke, 62 Max) to ensure exact temperature gradients in experiments. TEDs were connected to an oscilloscope (Tektronix, TDS2004C) for data collection and storage in a computer. To investigate TED's output voltage under strain, the TE tensile specimens were stretched to a certain strain value and then taped down on the hot plate. A resistance decade box (Extech, 380400) was parallelly connected to TEDs to measure the voltage across the known load resistor for estimating the generated power as well as power density.

*Thermal Imaging and Temperature Measurement*: A thermal imaging camera (FLIR-T621xx) was used to take Forward Looking Infrared (FLIR) images for thermoelectric devices. A 1-ampere current was applied to the TED to induce a change in temperature on the surface for active heating and cooling. The real-time temperature was recorded via FLIR Tools software. The current was applied for 180 s to investigate the change in temperature and the thermal regulation performance in the four different samples. Then the current was cut off to see how the residual heat affects the thermal interface layer.

*Wearable Electronics Applications*: For battery charging, TEDs were placed on the heat plate with a temperature gradient of 60 °C with respect to the room temperature and connected to a boost converter (MCRY-EVALKIT, MATRIX). The converted voltage was supplied to the coin cell battery (TS920E, Seiko Instruments) for 3 h and 30 min. The battery with a nominal voltage of 1.5 V was discharged to 1.2 V before the measurement to characterize the charging performance of the TEDs with and without the 3D soft architecture.

To light up the LED, Macro-TED with the soft architecture and the boost converter were serially connected and attached to the fabric. The integrated device was then worn on the forearm to demonstrate that the body heat can power the LED at room temperature. Similarly, harvested energy from body heat powered a low current temperature/humidity sensor (SPX-16618, Sparkfun) and a pressure/temperature sensor (SEN-11084, Sparkfun) separately. The conditions for these sensor demonstrations were an outside temperature of 6 °C and a relative humidity of 81%RH. The sensors were pressed using the index finger for 3 s twice, and the measured outcome was delivered to Arduino Uno. The sample rate was set to 1 s and the measured signals were combined after the measurements from two different sensors. A signed consent letter was obtained from the volunteer for wearing the stretchable thermoelectric generator.

## Supporting Information

Supporting Information is available from the Wiley Online Library or from the author.

## Acknowledgements

The authors acknowledge financial support from the National Science Foundation (CMMI-2306613), Meta, and The Boeing Company. Part of this work was conducted at the Molecular Analysis Facility, a National Nanotechnology Coordinated Infrastructure (NNCI) site at the University of Washington with partial support from the National Science Foundation (NNCI-1542101 and NNCI-2025489). The authors thank Nouryon for providing samples of Expancel thermoplastic microspheres.

## Conflict of Interest

The authors declare no conflict of interest.

## Data Availability Statement

The data that support the findings of this study are available from the corresponding author upon reasonable request.

## Keywords

3D printing, liquid metal, self-healing, stretchable electronics, thermoelectric

Received: May 18, 2024
Published online:

[1] Q. Zhang, K. Deng, L. Wilkens, H. Reith, K. Nielsch, *Nat. Electron.* **2022**, *5*, 333.
[2] J. Qiu, Y. Yan, T. Luo, K. Tang, L. Yao, J. Zhang, M. Zhang, X. Su, G. Tan, H. Xie, M. G. Kanatzidis, C. Uher, X. Tang, *Energy Environ. Sci.* **2019**, *12*, 3106.
[3] M. H. Malakooti, N. Kazem, J. Yan, C. Pan, E. J. Markvicka, K. Matyjaszewski, C. Majidi, *Adv. Funct. Mater.* **2019**, *29*, 1906098.
[4] J. Lee, D. Kim, H. Sul, S. H. Ko, *Adv. Funct. Mater.* **2021**, *31*, 2007376.
[5] S. Hong, Y. Gu, J. K. Seo, J. Wang, P. Liu, Y. S. Meng, S. Xu, R. Chen, *Sci. Adv.* **2019**, *5*, eaaw0536.
[6] S. J. Kim, H. E. Lee, H. Choi, Y. Kim, J. H. We, J. S. Shin, K. J. Lee, B. J. Cho, *ACS Nano* **2016**, *10*, 10851.
[7] M. Zadan, C. Chiew, C. Majidi, M. H. Malakooti, *Multifunctional Materials* **2021**, *4*, 012001.
[8] Q. Yang, S. Yang, P. Qiu, L. Peng, T. R. Wei, Z. Zhang, X. Shi, L. Chen, *Science* **1979**, *377*, 854.
[9] F. Suarez, D. P. Parekh, C. Ladd, D. Vashaee, M. D. Dickey, M. C. Öztürk, *Appl. Energy* **2017**, *202*, 736.
[10] K. Nan, S. D. Kang, K. Li, K. J. Yu, F. Zhu, J. Wang, A. C. Dunn, C. Zhou, Z. Xie, M. T. Agne, H. Wang, H. Luan, Y. Zhang, Y. Huang, G. J. Snyder, J. A. Rogers, *Sci. Adv.* **2018**, *4*, eaau5849.
[11] W. Ren, Y. Sun, D. Zhao, A. Aili, S. Zhang, C. Shi, J. Zhang, H. Geng, J. Zhang, L. Zhang, J. Xiao, R. Yang, *Sci. Adv.* **2021**, *7*, eabe0586.
[12] M. D. Dickey, *Adv. Mater.* **2017**, *29*, 1606425.
[13] Z. Xue, H. Song, J. A. Rogers, Y. Zhang, Y. Huang, *Adv. Mater.* **2020**, *32*, 1902254.
[14] V. Vallem, Y. Sargolzaeiaval, M. Ozturk, Y. C. Lai, M. D. Dickey, *Adv. Mater.* **2021**, *33*, 2004832.
[15] A. Haake, R. Tutika, G. M. Schloer, M. D. Bartlett, E. J. Markvicka, *Adv. Mater.* **2022**, *34*, 2200182.
[16] Y. Han, L. E. Simonsen, M. H. Malakooti, *Adv. Energy Mater.* **2022**, *12*, 2201413.
[17] P. Ramesh, Y. Sargolzaeiaval, T. Neumann, V. Misra, D. Vashaee, M. D. Dickey, M. C. Ozturk, *npj Flexible Electron.* **2021**, *5*, 5.
[18] P. Won, C. S. Valentine, M. Zadan, C. Pan, M. Vinciguerra, D. K. Patel, S. H. Ko, L. M. Walker, C. Majidi, *ACS Appl. Mater. Interfaces* **2022**, *14*, 55028.
[19] M. D. Bartlett, N. Kazem, M. J. Powell-Palm, X. Huang, W. Sun, J. A. Malen, C. Majidi, *Proc Natl Acad Sci U S A* **2017**, *114*, 2143.

[20] J. Ma, F. Krisnadi, M. H. Vong, M. Kong, O. M. Awartani, M. D. Dickey, *Adv. Mater.* **2023**, *35*, 2205196.
[21] M. H. Malakooti, M. R. Bockstaller, K. Matyjaszewski, C. Majidi, *Nanoscale Adv* **2020**, *2*, 2668.
[22] F. C. Liang, B. C. K. Tee, *Adv. Funct. Mater.* **2024**, *34*, 2400284.
[23] G. G. Guymon, M. H. Malakooti, *J. Poly. Science* **2022**, *60*, 1300.
[24] C. Chiew, M. H. Malakooti, *Compos. Sci. Technol.* **2021**, *208*, 108752.
[25] M. Zadan, M. H. Malakooti, C. Majidi, *ACS Appl. Mater. Interfaces* **2020**, *12*, 17921.
[26] M. Zadan, D. K. Patel, A. P. Sabelhaus, J. Liao, A. Wertz, L. Yao, C. Majidi, *Adv. Mater.* **2022**, *34*, 2200857.
[27] B. Lee, H. Cho, K. T. Park, J. S. Kim, M. Park, H. Kim, Y. Hong, S. Chung, *Nat. Commun.* **2020**, *11*, 5948.
[28] Y. Sato, S. Terashima, E. Iwase, *Micromachines (Basel)* **2023**, *14*, 218.
[29] S. H. Jeong, F. J. Cruz, S. Chen, L. Gravier, J. Liu, Z. Wu, K. Hjort, S. L. Zhang, Z. B. Zhang, *ACS Appl. Mater. Interfaces* **2017**, *9*, 15791.
[30] Y. Shi, X. Lü, Q. Xiang, J. Li, X. Shao, W. Bao, *Energy Convers Manag* **2022**, *253*, 115167.
[31] T. Koshi, A. Takei, T. Nobeshima, S. Kanazawa, K. Nomura, S. Uemura, *Flexible Printed Electron.* **2022**, *9*, 015009.
[32] Y. Yang, H. Hu, Z. Chen, Z. Wang, L. Jiang, G. Lu, X. Li, R. Chen, J. Jin, H. Kang, H. Chen, S. Lin, S. Xiao, V. Zhao, R. Xiong, J. Shi, Q. Zhou, S. Xu, Y. Chen, *Nano Lett* **2020**, *20*, 4445.
[33] K. Fukuie, Y. Iwata, E. Iwase, *Micromachines (Basel)* **2018**, *9*, 315.
[34] M. H. Jeong, A. Sanger, S. B. Kang, Y. S. Jung, I. S. Oh, J. W. Yoo, G. H. Kim, K. J. Choi, *J Mater Chem A Mater* **2018**, *6*, 15621.
[35] T. S. Lee, S. Nam, J. G. Oh, E. H. Suh, J. Jung, H. Oh, Y. J. Jeong, J. Jang, *Chem. Eng. J.* **2023**, *455*, 140925.
[36] N. Wen, Z. Fan, S. Yang, Y. Zhao, C. Li, T. Cong, H. Huang, J. Zhang, X. Guan, L. Pan, *Chem. Eng. J.* **2021**, *426*, 130816.
[37] N. Wen, Z. Fan, S. Yang, Y. Zhao, T. Cong, S. Xu, H. Zhang, J. Wang, H. Huang, C. Li, L. Pan, *Nano Energy* **2020**, *78*, 105361.
[38] T. Sun, B. Zhou, Q. Zheng, L. Wang, W. Jiang, G. J. Snyder, *Nat. Commun.* **2020**, *11*, 572.
[39] Y. Zheng, X. Han, J. Yang, Y. Jing, X. Chen, Q. Li, T. Zhang, G. Li, H. Zhu, H. Zhao, G. J. Snyder, K. Zhang, *Energy Environ. Sci.* **2022**, *15*, 2374.
[40] Y. Hou, Y. Yang, Z. Wang, Z. Li, X. Zhang, B. Bethers, R. Xiong, H. Guo, H. Yu, *Adv. Sci.* **2022**, *9*, 2103574.
[41] Y. Wang, Z. Zhou, J. Zhou, L. Shao, Y. Wang, Y. Deng, *Adv. Energy Mater.* **2022**, *12*, 2102835.
[42] B. Wu, W. Wei, Y. Guo, W. Hou Yip, B. Kang Tay, C. Hou, Q. Zhang, Y. Li, H. Wang, *Chem. Eng. J.* **2023**, *453*, 139749.
[43] P. Won, S. Coyle, S. H. Ko, D. Quinn, K. J. Hsia, P. LeDuc, C. Majidi, *Adv. Healthcare Mater.* **2023**, *12*, 2202430.
[44] R. M. Chin, Y. Han, M. H. Malakooti, *Adv. Mater. Technol.* **2023**, *9*, 2301324.
[45] W. Zhou, K. Yamamoto, A. Miura, R. Iguchi, Y. Miura, K. I. Uchida, Y. Sakuraba, *Nat. Mater.* **2021**, *20*, 463.
[46] Y. Dubi, M. D. Ventra, *Nano Lett.* **2009**, *9*, 97.
[47] F. J. DiSalvo, *Science* **1979**, *285*, 703.
[48] G. J. Snyder, A. H. Snyder, *Energy Environ. Sci.* **2017**, *10*, 2280.
[49] I. T. Witting, T. C. Chasapis, F. Ricci, M. Peters, N. A. Heinz, G. Hautier, G. J. Snyder, *Adv. Electron. Mater.* **2019**, *5*, 1800904.
[50] Y. Saberi, S. A. Sajjadi, *J. Alloys Compd.* **2022**, *904*, 163918.
[51] M. Tavakoli, M. H. Malakooti, H. Paisana, Y. Ohm, D. Green Marques, P. Alhais Lopes, A. P. Piedade, A. T. de Almeida, C. Majidi, *Adv. Mater.* **2018**, *30*, 1801852.
[52] N. Lu, C. Lu, S. Yang, J. Rogers, *Adv. Funct. Mater.* **2012**, *22*, 4044.
[53] E. J. Markvicka, M. D. Bartlett, X. Huang, C. Majidi, *Nat. Mater.* **2018**, *17*, 618.
[54] R. Tutika, A. B. M. T. Haque, M. D. Bartlett, *Commun Mater* **2021**, *2*, 64.
[55] Y. Zhao, Y. Ohm, J. Liao, Y. Luo, H.-Y. Cheng, P. Won, P. Roberts, M. R. Carneiro, M. F. Islam, J. H. Ahn, L. M. Walker, C. Majidi, *Nat. Electron.* **2023**, *6*, 206.
[56] M. D. Bartlett, M. D. Dickey, C. Majidi, *NPG Asia Mater* **2019**, *11*, 21.